ACS Catalysis

Research Article

Cite This: ACS Catal. 2018, 8, 6203−6215

pubs.acs.org/acscatalysis

Low-Temperature CO_2 Methanation over CeO_2-Supported Ru Single Atoms, Nanoclusters, and Nanoparticles Competitively Tuned by Strong Metal−Support Interactions and H-Spillover Effect

Yu Guo,[†] Sheng Mei,[†] Kun Yuan,[†] De-Jiu Wang,[†] Hai-Chao Liu,*[,‡] Chun-Hua Yan,[†] and Ya-Wen Zhang*[,†]

[†]Beijing National Laboratory for Molecular Sciences, State Key Laboratory of Rare Earth Materials Chemistry and Applications, PKU-HKU Joint Laboratory in Rare Earth Materials and Bioinorganic Chemistry, and [‡]Beijing National Laboratory for Molecular Sciences (BNLMS), State Key Laboratory for Structural Chemistry of Stable and Unstable Species, College of Chemistry and Molecular Engineering, Peking University, Beijing 100871, People's Republic of China

Supporting Information

ABSTRACT: CO_2 hydrogenation for the acquisition of value-added chemicals is an economical means to deal with the CO_2-relevant environmental problems, among which CO_2 reduction to CH_4 is an excellent model reaction for investigating the initial steps of CO_2 hydrogenation. For the supported catalysts commonly used in such reactions, the tailoring of the interfacial effect between metal centers and supporting materials so as to obtain superior low-temperature CO_2 methanation performance is a significant but challenging subject. In this work, we altered the size regimes of the Ru deposits in Ru/CeO_2 assemblies and uncovered the competitive relationship between the strong metal−support interactions (SMSI) and the H-spillover effect in determining the methanation activities by some ex situ and in situ spectroscopic techniques coupled with density functional theory (DFT) calculations. For CeO_2 nanowire supported single Ru atoms, Ru nanoclusters (ca. 1.2 nm in size), and large Ru nanoparticles (ca. 4.0 nm in size), the nanoclusters show the most outstanding low-temperature CO_2 methanation activity and 98−100% selectivity, with a turnover frequency (TOF) of 7.41×10^{-3} s^{-1} at 190 °C. The negative CO_2 reaction order decreases their absolute values from single atoms to nanoclusters and turns positive in nanoparticles, while the positive H_2 reaction order follows the reverse tendency. In situ DRIFTS measurements demonstrate that the dominant reaction pathway is the CO route, in which metal carbonyls are the critical intermediates and the active sites are those Ce^{3+}−OH sites and Ru sites near the metal−support interfaces in charge of CO_2 dissociation and carbonyl hydrogenation, respectively. Meanwhile, the strongest SMSI and H-spillover effect are respectively encountered in supported single Ru atoms and large Ru nanoparticles, with the activation of metal carbonyls and the dehydration of the support surfaces suppressed correspondingly. The two factors reach a balance in CeO_2-supported Ru nanoclusters, and the methanation activity is therefore maximized. A mechanistic understanding of the interfacial effect in tuning the CO_2 methanation activities would shed light on the ingenious design of the CO_2 hydrogenation catalysts to utilize the SMSI and H-spillover effect to an appropriate degree and avoid their possible suppressions that would take place in extreme cases.

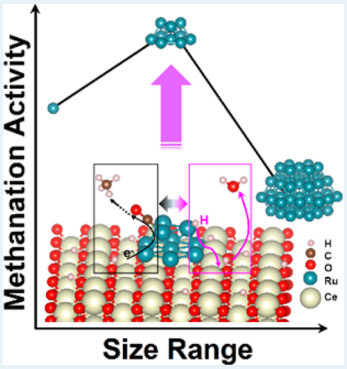

KEYWORDS: *CO_2 hydrogenation, strong metal−support interactions, H-spillover effect, single atom, nanocluster, nanoparticle*

1. INTRODUCTION

CO_2 capture and recycling (CCR) is an effective approach to coping with the increasingly severe greenhouse effect. A series of value-added chemicals including CO, CH_4, CH_3OH, HCOOH, C_2H_4, and C_{2+} hydrocarbons can be obtained via heterogeneous catalysis.[1] Recently developed CO_2 electro- and photoreductions shed light on such catalytic reactions,[2−4] while CO_2 thermal reduction with H_2 by heterogeneous catalysts is still the method with the most in-depth investigation and development.[5,6] The hydrogenation catalysts are always designed as supported catalysts to anchor the active metal components on the high-surface-area supports,[7] preventing the metal particles from agglomeration.[8] The supported assemblies are always regarded as the metal−oxide heterojunctions,[9] where the metal−support interfaces play pivotal roles in governing the electronic and chemical properties of the catalysts and the surface chemistry in the hydrogenation process. Despite the varied hydrogenation products, the facile activation of CO_2 and H_2 is the prerequisite for achieving considerable catalytic activities and selectivities, and the interfacial effect is in direct correlation with the charge transfer and mass transport in the activation of reactant molecules. Therefore, how to tailor such interfacial effects to obtain superior catalytic performance in CO_2 hydrogenation is a very attractive but challenging subject.

Received: December 27, 2017
Revised: April 23, 2018
Published: May 24, 2018

DOI: 10.1021/acscatal.7b04469
ACS Catal. 2018, 8, 6203−6215

The interfacial effects in supported metal catalysts are affected by a series of structural factors including the particle size[5,10−12] and the alloying degree[13] of the active metals and the surface area,[14] the crystal planes,[15] the Lewis acidity or reducibility,[16,17] and the porosity[18] of the supports, which have all been demonstrated to readily tune the activities and selectivities in CO_2 hydrogenation. Among them, the size effect is the most debated and confusing matter, for the optimized sizes of metal particles vary greatly in different catalytic assemblies: for instance, 15 nm for Rh/γ-Al_2O_3,[19] 17 nm for Rh/TiO_2,[20] and 2.5 nm for Ru/TiO_2[21] in CO_2 methanation. In essence, CO_2 methanation is an excellent model reaction to probe into the initial steps of CO_2 hydrogenation, for the generation of CH_4 and CO involves the fundamental steps of CO_2 dissociation and hydrogenation,[22−24] after which the formation of C−C bonds becomes possible, and the reaction proceeds at atmospheric pressure and low temperatures, in contrast to the harsh reaction conditions for other products. The size effect in CO_2 methanation thereby needs systematic investigation in extended size regimes.

More recently, supported single-atom catalysts have been developed to work remarkably in oxidation and hydrogenation reactions[25] such as Pt_1/Fe_3O_4 for CO oxidation[26] and Rh_1/ZSM-5[27] and Fe_1/SiO_2[28] for methane oxidation to acetic acid and olefins. The isolated active sites guarantee that the adsorbed species react with high selectivity and that the side reactions are largely suppressed.[28] Nanoclusters (typically smaller than 2−3 nm) and large nanoparticles (3−20 nm)[29] provide more than one active site on which the conversion of adsorbed species could take place over several sites. Large nanoparticles are representative of fine crystallinity and less affected geometric and electronic structures, while nanoclusters gain both the characters of versatile geometric and electronic structures and multiple neighboring sites.[30,31]

Distinct interfacial effects underlie the assemblies with active metal components in different size regimes and finally give rise to the catalytic contrasts. The interfacial effects in supported hydrogenation catalysts primarily consist of strong metal−support interactions (SMSI) and H-spillover effects. The former was first found by Tauser et al.[32,33] from the suppression of H_2 chemisorption for precious metals supported on TiO_2[34] and differs greatly in type and degree from the other metal−support interactions.[35−37] Having been studied and replenished over the past 40 years, SMSI has been extended to group 8−10 metals on reducible oxides[38−42] and its nature is interpreted as the electronic interaction of charge transfer[38−40] and the chemical interaction of encapsulation.[41,43] It also has been argued to account for numerous structure−reactivity relationships[44] of methanation reactions. Li et al.[45] pointed out that the chemical state of Ir species is modulated by the CeO_2 support in Ir/CeO_2 and the metallic Ir is advantageous to the activation and dissociation of adsorbed CO intermediates in CO_2 methanation, thus contributing to the relatively higher CH_4 selectivity. Behm et al.[46] discovered that the partial overgrowth of Ru particles by small TiO_x islands in Ru/TiO_2 leads to enhanced CO adsorption strength, which finally brings about the high selectivity for CO methanation but low activity for CO_2 dissociation. In a word, the electronic and chemical interactions of SMSI have all been demonstrated to play vital roles in the processes related to the CO_2 methanation. H-spillover effects also readily occur in metal oxide supported metal catalysts,[47,48] which has been proved by Ruiz et al.[49] in Rh/γ-Al_2O_3 to help activate adsorbed CO groups on Pd/γ-Al_2O_3 mechanically mixed with Rh/γ-Al_2O_3. A similar phenomenon was encountered in SiO_2-supported Pt and Co nanoparticles in close proximity, where the H atoms dissociated on Pt sites could migrate to the Co sites to facilitate the removal of surface oxides and the regeneration of Co active sites.[50] Hence, the SMSI and H-spillover effects coexist in the supported methanation catalysts, whereas how the two interfacial effects exert synergistic influences on the methanation performances is still unknown.

Herein, we demonstrate the notably different CO_2 methanation activities of CeO_2 nanowire supported single Ru atoms, Ru nanoclusters (ca. 1.2 nm in size), and Ru nanoparticles (ca. 4.0 nm in size), which have been proved highly active at low temperatures.[15] Ru/CeO_2 catalysts in different size regimes with varied intensities of SMSI and H-spillover effects were investigated via a series of ex situ and in situ spectroscopic techniques combined with density functional theory (DFT) calculations, and the SMSI and H-spillover effects were revealed to display a competitive relationship to jointly govern the methanation activity.

2. EXPERIMENTAL SECTION

2.1. Chemicals. $CeCl_3·7H_2O$ (AR, Sinopharm Chemical Corp., People's Republic of China), $NdCl_3·6H_2O$ (AR, Beijing HWRK Chemical Corp., People's Republic of China), $GdCl_3·6H_2O$ (J&K Chemical Corp., People's Republic of China), $RuCl_3$ (AR, Sinopharm Chemical Corp., People's Republic of China), NaCl (AR), NaOH (AR), and $NaBH_4$ (AR) were used as the starting materials.

2.2. Synthesis of Ru/CeO_2 NWs. $Ce(OH)_3$ nanowires were synthesized via the reported hydrothermal method.[42,51] A 279 mg portion of $CeCl_3·7H_2O$, 3.6 g of NaOH, and 523 mg of NaCl were dissolved and mixed in 15 mL of water, and this mixture was placed in a 25 mL Teflon-lined autoclave and heated at 180 °C for 24 h. The nanowires were collected by centrifugation, washed two times with deionized water, and redispersed in 12 mL of water with the pH value adjusted to 8.0−8.5. Nd- and Gd-doped $Ce(OH)_3$ nanowires were obtained following the same steps except that 251.5 mg of $CeCl_3·7H_2O$ and 26.9 mg of $NdCl_3·6H_2O$ or 27.9 mg of $GdCl_3·6H_2O$ were added instead of 279 mg of $CeCl_3·7H_2O$.

Ru/CeO_2 composites were fabricated by the impregnation method. CeO_2-supported Ru single atoms (denoted as Ru(SA)/CeO_2) were obtained by adding 490 μL of $RuCl_3$ solution (0.075 mol L^{-1}) to the suspension of $Ce(OH)_3$ nanowires and stirring the mixture for 2 h at room temperature, while in the preparation of Ru nanoclusters (denoted as Ru(NC)/CeO_2), 970 μL of the $RuCl_3$ solution was added and the mixture was stirred for 5 h. The stirring time was the critical parameter to control the adsorption extent of the hydrated Ru cations and the final size of the Ru deposits. In addition, Ru nanoparticles (denoted as Ru(NP)/CeO_2) were synthesized via a fast reduction with $NaBH_4$ added drop by drop. The three products were washed twice with deionized water and then dried at 70 °C for at least 12 h, after which the products were converted to Ru/CeO_2 assemblies. The samples of Ru(SA)/CeO_2, Ru(NC)/CeO_2, and Ru(NP)/CeO_2 were all prepared with good reproducibility.

2.3. Characterization. Transmission electron microscopy (TEM), high-resolution transmission electron microscopy (HRTEM), high-angle annular dark field scanning transmission electron microscopy (HAADF-STEM), and element mapping were conducted on a FEG-TEM instrument (JEM-2100F,

DOI: 10.1021/acscatal.7b04469
ACS Catal. 2018, 8, 6203−6215

JEOL, Japan) operated at 200 kV. Aberration-corrected high-angle annular dark field scanning transmission electron microscopy (cs-corrected HAADF-STEM) and element mapping were obtained from a FEI TITAN aberration-corrected Themis instrument operated at 300 kV. The samples sparsely dispersed in ethanol were dropped on copper grids coated with amorphous carbon membranes and dried for TEM observations. The size distribution of Ru components was analyzed on the basis of the statistics of over 50 deposits. The dispersion of Ru deposits (D) was further calculated from the equation[52]

$$D = \frac{6V/a}{d} = \frac{6Mn_s}{\rho N_A d} \quad (1)$$

where V denotes the volumes occupied by a Ru atom in the bulk of the metal (Å^3), a denotes the surface area occupied by a Ru atom on the polycrystalline surface (Å^2), d denotes the mean particle size (Å), M denotes the atomic mass (g mol^{-1}), n_s denotes the mean number of atoms in the exposed plane (m^{-2}), ρ denotes the mass density (g cm^{-3}), and N_A is Avogadro's number (6.02×10^{23} mol^{-1}). For *hcp* Ru exposed (001) surfaces, eq 1 is converted to

$$D = \frac{12.9}{d} \quad (2)$$

The loading amount of Ru on CeO_2 was analyzed from inductively coupled plasma objective emission spectroscopy (ICP-OES) on a Profile Spec ICP-OES spectrometer (Leeman, USA). X-ray photoelectron spectroscopy (XPS) data were acquired on an Axis Ultra XPS spectrometer (Kratos, U.K.) with Al Kα radiation operated at 225 W. The binding energies were calibrated by the C 1s peak at 284.8 eV. Raman spectra were collected on a Jobin-Yvon HR800 laser Raman microscope with 488 nm laser excitation. X-ray absorption near edge structure (XANES) and extended X-ray absorption fine structure (EXAFS) analyses of the Ru K edge (22117 eV) were carried out on the BL14W1 beamline of the Shanghai Synchrotron Radiation Facility (SSRF) at 3.5 GeV with a maximum current of 300 mA. A Si (111) double-crystal monochromator was utilized. The IFFEFIT 1.2.11 data analysis package (Athena, Artemis) was used for data extraction and curve fitting.

Temperature-programmed hydrogen reduction (H_2-TPR) and desorption (H_2-TPD) were conducted on a Xianquan TP-5080 adsorption apparatus. In H_2-TPR, the samples (50 mg) were heated from 30 to 800 °C with a heating rate of 10 °C/min under 30 mL/min of flowing 5% H_2/N_2. In H_2-TPD, the samples were pretreated at 350 °C under 5% H_2/N_2 for 2 h, purged with N_2 for 0.5 h, and then cooled to 30 °C to adsorb H_2. After they were purged with N_2 for 30 min, the samples were heated to 800 °C at a rate of 10 °C/min. In situ diffuse reflectance infrared Fourier transform spectroscopy (DRIFTS) was measured on a Bruker TENSOR 27 spectrometer. The samples were exposed to a gas mixture of CO_2, H_2, and He with a total flow rate of 40 mL/min in a Praying Mantis DRIFTS cell. Prior to the IR measurements, the samples were pretreated in flowing 5% H_2/He at 300 °C for 30 min.

2.4. Catalytic Tests. The CO_2 hydrogenation reactions took place in a fixed-bed reactor at atmospheric pressure. A 50 mg portion of the catalyst was mixed with quartz sand (40−70 mesh) and loaded in a quartz tube (1 cm in diameter). Prior to the catalytic test, the samples were in situ activated in H_2 at 350 °C for 120 min. The reactant gas consisted of CO_2 (2 mL/min), H_2 (8 mL/min), and He (30 mL/min). The outlet gas mixture was analyzed online by an Agilent 7890A gas chromatograph equipped with a TCD detector and a carbon molecular sieve column (Carboxen 1000, Supelco, USA). The methanation activity was assessed via turnover frequency (TOF), which was normalized by the loading amount and the dispersion of Ru deposits on CeO_2 supports:

$$\mathrm{TOF} = \frac{F_{CO_2} X_{CH_4} M}{WDx} \quad (3)$$

where F_{CO_2} denotes the molar number of CO_2 molecules at the reaction temperature per unit time (mol s^{-1}), X_{CH_4} denotes the proportion of CH_4 molecules in the outflow, M is the atomic mass of Ru (g mol^{-1}), W denotes the weight of the catalyst packed into the reactor (g), D denotes the dispersion of Ru deposits, and x denotes the loading amount of Ru deposits on the CeO_2 supports.

2.5. First-Principles Calculations. DFT calculations were performed with the VASP package. The exchange-correlation energy functional was described in the Perdew−Burke−Ernzerhof (PBE) generalized gradient approximation (GGA). The k point was set to the γ point in the Brillouin zone. The atoms were presented by projector augmented-wave (PAW) pseudopotentials. The kinetic energy cutoff was 500 eV for the plane-wave basis set. CeO_2 supercells ($2 \times 2 \times 2$) were built, with (110) surfaces exposed and the bottom two layers fixed. Vacuum layers (15 Å) were added to the CeO_2 slab, and 5 eV of U was imposed to the Ce 4f orbitals. Each structure was relaxed until the residual force was smaller than 0.02 eV/Å.

3. RESULTS AND DISCUSSION

3.1. Preparation of Ru/CeO_2 Assemblies and Catalytic Tests of CO_2 Methanation. According to the TEM observations, the well-crystallized CeO_2 nanowires obtained via the hydrothermal method had a length of 1−3 μm and a width of 10−80 nm. In particular, the $Ce(OH)_3$ intermediates formed under subcritical hydrothermal conditions were transformed into CeO_2 nanowires[51] in the air, which preferably grew along the [110] direction (Figure S1b) and were mainly enclosed by the (110) surfaces that have been observed in CeO_2 nanorods,[53] nanowires,[51] and nanosheets.[54] The size and coordination structure of the Ru deposits were determined by a combination of HRTEM, STEM, and XAFS analyses (Figures 1 and 2, Figure S2, and Table 1). Owing to the limitation of resolution, the bright dots of Ru atoms cannot be observed in the HAADF-STEM image of Ru(SA)/CeO_2, but EDS mapping proves the existence of highly dispersed Ru species on the CeO_2 nanowires (Figure 1a,b). The corresponding Fourier transform of the EXAFS profile was fitted by two Ru−O paths (Figure S3a) and showed no signal at ca. 2.4 Å (Figure 2b) which is representative of Ru−Ru coordination (Figure S3b,c), indicating that the Ru element of Ru(SA)/CeO_2 was dispersed as single atoms. For Ru(NC)/CeO_2, some nanoclusters were found to be located on the edge of the nanowires, and a comparison between the HAADF-STEM image and the EDS mapping certifies that the nanoclusters were composed of Ru atoms (Figure 1c,d). It is apparent from the element mapping result that Ru species were more aggregated in comparison to those of Ru(SA)/CeO_2, and the mean size of the nanoclusters was 1.18 ± 0.25 nm (Figure S2b and Table 1) with ca. 100 Ru atoms. The adhered Ru nanoclusters were crystallized to some

DOI: 10.1021/acscatal.7b04469
ACS Catal. 2018, 8, 6203−6215

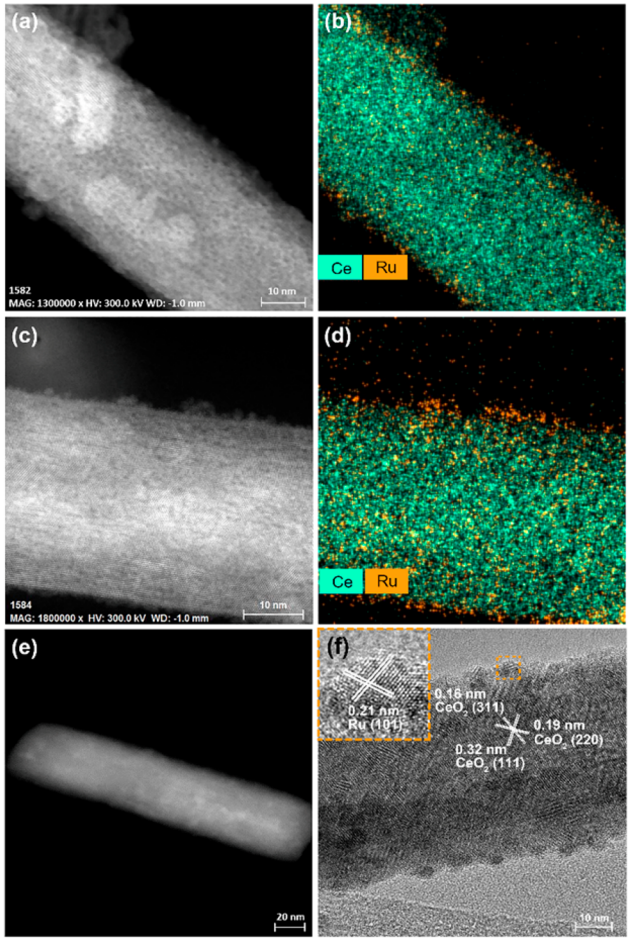

Figure 1. Cs-corrected (a, c) HAADF-STEM images and (b, d) corresponding element maps of $Ru(SA)/CeO_2$ and $Ru(NC)/CeO_2$. (e) HAADF-STEM and (f) HRTEM images of $Ru(NP)/CeO_2$. The inset panel in (f) is the magnified HRTEM image of Ru nanoparticles showing hexagonal Ru (101) lattice fringes.

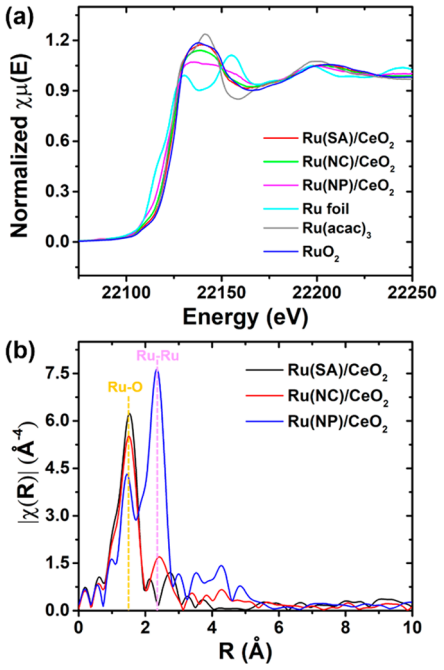

Figure 2. (a) XANES curves of the three catalysts after H_2 reduction and the reference curves of Ru foil, $Ru(acac)_3$, and RuO_2. (b) Fourier transform of the EXAFS signals of the reduced catalysts. The shell radii (R) of Ru−O and Ru−Ru are marked in Figure 2b by yellow and pink dashed lines.

Table 1. Structural Information of Ru/CeO_2 Assemblies

sample	Ru (wt %)	Ru size (nm)	D (%)	shell	CN[a]
$Ru(SA)/CeO_2$	0.89		100	Ru−O	4.5 ± 1.3
$Ru(NC)/CeO_2$	2.56	1.18 ± 0.25	100	Ru−O	4.2 ± 0.9
				Ru−Ru	2.4 ± 1.2
$Ru(NP)/CeO_2$	3.70	4.01 ± 0.80	32	Ru−O	3.3 ± 1.3
				Ru−Ru	3.8 ± 0.7

[a]For details, see Table S1 and Figure S3 in the Supporting Information.

Table 2. Kinetic Parameters of Ru/CeO_2 Catalysts

sample	TOF at 190 °C (s^{-1})	E_a (kJ mol^{-1})	CO_2 reaction order[a]	H_2 reaction order
$Ru(SA)/CeO_2$	4.59×10^{-3}	82.4	−0.50	0.30
$Ru(NC)/CeO_2$	7.41×10^{-3}	79.4	−0.42	0.40
$Ru(NC)/Ce_{0.9}Nd_{0.1}O_\delta$	4.52×10^{-3}	79.5	−0.32	0.43
$Ru(NC)/Ce_{0.9}Gd_{0.1}O_\delta$	5.90×10^{-3}	79.6	−0.33	0.31
$Ru(NP)/CeO_2$	5.30×10^{-4}	77.4	0.74	0.67

[a]CO_2 and H_2 reaction orders were obtained at 160 °C with a conversion rate of less than 10%.

degree, and the lattice fringes of hexagonal Ru (101) could be distinguished in some clusters on the edges of nanowires (Figure S2a). The Ru particles in $Ru(NP)/CeO_2$ exhibited distinct lattice fringes representative of fine crystallinity (Figure 1f), with a mean size of 4.01 ± 0.80 nm (Figure S2d and Table 1). Accordingly, the dispersions of Ru deposits (D) in $Ru(NC)/CeO_2$ and $Ru(NP)/CeO_2$ were calculated from their mean sizes via eq 1 (Table 1). The single Ru atoms and the Ru atoms of $Ru(NC)/CeO_2$ (ca. 1.2 nm) were all 100% dispersed, while 32% of the Ru atoms in Ru nanoparticles (ca. 4.0 nm) were exposed. The Ru K edge XANES curves of the three catalysts give the oxidation states of the Ru species: that is, highly oxidized single Ru atoms for $Ru(SA)/CeO_2$, partially reduced Ru clusters for $Ru(NC)/CeO_2$, and largely reduced Ru particles for $Ru(NP)/CeO_2$ (Figure 2a and Table 1).

The three catalysts exhibited distinct differences in the CO_2 methanation activities, while the selectivities of CH_4 all reached 98−100% (Figure S4a), which is in accord with the superior methanation activity of Ru.[7] As a comparison, the CeO_2 support showed little activity toward CO_2 hydrogenation and no CH_4 selectivity under our experimental conditions (Figure S4a). Among the three catalysts, $Ru(NC)/CeO_2$ showed the highest activity, with a TOF of 7.41×10^{-3} s^{-1} at 190 °C (Table 2), which is 1.6 times higher than the TOF of $Ru(SA)/CeO_2$ and 14.0 times higher than that of $Ru(NP)/CeO_2$. The methanation activities of the catalysts in this work are all much higher than the values of Ru/CeO_2 catalysts reported in other literature works[14,15] under similar reaction conditions, possibly due to the disordered atomic arrangement (Figure S2a,c) of the

DOI: 10.1021/acscatal.7b04469
ACS Catal. 2018, 8, 6203−6215

support surface caused by the direct impregnation of the as-prepared $Ce(OH)_3$ nanowires in the solution of Ru precursor during our catalyst preparation. Further kinetic tests demonstrated that the activation energy E_a decreased from 82.4 kJ mol^{-1} to 77.4 kJ mol^{-1} with an increase in the size regime of Ru deposits from single atom to large particles (Figure 3 and Table 2). What the size regime of Ru deposits affects directly is the metal–support interface area; therefore, the active sites should be located at the interface to account for the variations in E_a. On the other hand, the effect of the CeO_2 support was investigated by carrying out the same tests on rare-earth (Nd, Gd)-doped Ru(NC)/CeO_2 while the Ru deposits were kept in the same size regime (Figure S5). CeO_2 always works in redox reactions with the participation of active lattice oxygen atoms and defect sites.[55] The nonequivalent doping of CeO_2 support would introduce a mass of oxygen vacancies, as can be detected by Raman spectroscopy (Table S2). The methanation activities of the doping samples followed the sequence undoped > Gd-doped > Nd-doped (Figure 3), and the values of E_a were nearly unaffected (Table 2). The size regime of Ru deposits clearly exerts a more evident effect on the activities; thus, the rate-determining step is bound to take place on the Ru deposits and large Ru particles are in favor of such a step. In terms of catalytic stability, the three catalysts had little difference, all showing 20% losses of CH_4 production rates after 500 min of reaction at 220 °C (Figure S4b). In addition, the size of Ru nanoclusters in Ru(NC)/CeO_2 after the stability test was measured to be 1.35 ± 0.23 nm, which merely increased 14% in comparison to the original cluster size and indicates the good stability of this catalyst in long-term catalytic tests (Figure S6).

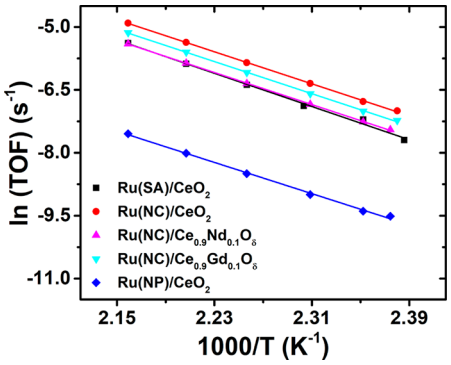

Figure 3. Arrhenius plot of Ru/CeO_2 catalysts. The activities were recorded at the second catalytic cycle and after stabilization for 1 h at each temperature point. The Arrhenius plots were measured from 140 to 190 °C to ensure that the conversion of CO_2 was less than 10%. TOF was normalized per exposed surface Ru atom, and the percent of exposed Ru atoms (Ru dispersion) was calculated on the basis of the mean size of Ru deposits. WHSV = 4800 mL g_{cat}^{-1} h^{-1}.

The apparent reaction orders of CO_2 were negative on Ru(SA)/CeO_2 and Ru(NC)/CeO_2 (Table 2), and the absolute value decreased from −0.50 to −0.42, which indicates some strongly adsorbed intermediate derived from CO_2 on the catalyst surface and consequently hinders the reaction; such a hindering effect weakened from Ru(SA)/CeO_2 to Ru(NC)/CeO_2. From Ru(NC)/CeO_2 to Ru(NP)/CeO_2, the CO_2 reaction order even turned into the positive value of 0.74. Thus, the hindrance of the carbon-containing intermediate is completely eliminated in Ru(NP)/CeO_2. The tendency is consistent with the reduction of activation energies (Table 2), thereby proving that the rate-determining step in this reaction is the conversion of certain carbon-containing intermediates on Ru sites. On the other hand, the reaction orders of H_2 were all positive and increased from 0.30 to 0.67 with the increase of the Ru size regime, suggesting the weighted dependence of methanation activities on the H_2 partial pressure from Ru(SA)/CeO_2 to Ru(NP)/CeO_2.

3.2. SMSI in the Opposite Variation of H-Spillover Effects. With the active sites confirmed to be located in the interface via kinetic measurements, the interfacial effects between the active Ru component and the CeO_2 support were brought forth to account for the activity difference of the Ru/CeO_2 catalysts in varied size regimes. The interfacial effects in the literature[31] have been summarized to include charge transfer, encapsulation, surface reconstruction, spillover, perimeter activation, synergistic interaction, and so on, among which charge transfer corresponds to the electronic interaction of SMSI and encapsulation and surface reconstruction belong to the chemical counterpart. From previous studies on the structure–reactivity relationships of CO_2 hydrogenation,[45,46,49,50] both SMSI and H-spillover effects have been discussed individually to have strong effects on the hydrogenation performances. Hence, we started the investigation of interfacial effects from these two aspects in this work. Raman and XPS spectroscopy were utilized to characterize the SMSI underlying the supported assemblies.

For the Raman signal of CeO_2, defect sites in the lattices would lead to a D mode at 598 cm^{-1}, which represents the Frenkel-type oxygen vacancies created by the relocation of oxygen anions from tetrahedral sites to octahedral sites,[56] in addition to the intrinsic F_{2g} mode at 465 cm^{-1} (Figure 4). The intensity ratio $I(D)/I(F_{2g})$ thus represents the relative concentration of oxygen vacancies in the CeO_2 lattices. Apart from Raman peaks at 465 and 598 cm^{-1}, there were two other peaks at 700 and 970 cm^{-1}, which could be assigned to the asymmetric structure of Ru–O–Ce.[15,57] The intensity ratio of the peaks attributed to Ru–O–Ce (denoted as I(Ru–O–Ce)) and intrinsic F_{2g} mode, I(Ru–O–Ce)/$I(F_{2g})$, can be used to

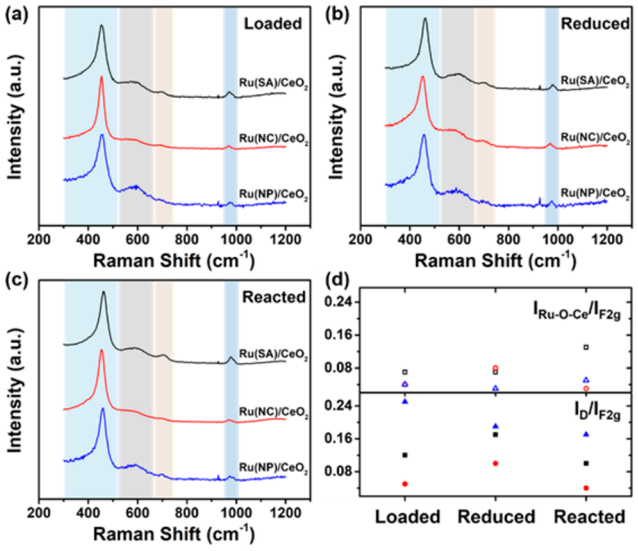

Figure 4. Raman spectra of differently sized Ru/CeO_2 catalysts once (a) loaded, (b) H_2 reduced, and (c) reacted. (d) $I_{Ru-O-Ce}/I_{F2g}$ and I_D/I_{F2g} values of Ru(SA)/CeO_2 (black squares), Ru(NC)/CeO_2 (red circles), and Ru(NP)/CeO_2 (blue triangles) in the cases of (a)–(c).

DOI: 10.1021/acscatal.7b04469
ACS Catal. 2018, 8, 6203–6215

represent the relative density of interfacial bonding (Figure 4d and Table S2). It is obvious that the three catalysts with different Ru sizes displayed distinct oxygen vacancy concentrations and that Ru(NC)/CeO_2 had the lowest concentration. There is no positive correlation between the methanation activity and the concentration of oxygen vacancy; thus, the rate-determining step is again proved to take place on the Ru sites rather than the oxygen vacancies. In spite of this, the oxygen vacancies all decreased greatly after CO_2 methanation (Figure 4d and Table S2), suggesting that the oxygen vacancies still actively participate in the methanation process. On the other hand, the density of Ru−O−Ce interfacial bonding directly reflects the chemical interaction of SMSI between Ru deposits and CeO_2 supports. The most extensive interfacial bonding was encountered in Ru(SA)/CeO_2 all along the reduction and methanation process, while the interfacial bonding intensity of Ru(NC)/CeO_2 was generally higher than that of Ru(NP)/CeO_2, indicating the weakened chemical interaction from CeO_2-supported single Ru atoms to large particles. In addition, the interfacial bonding after the reaction increased in Ru(SA)/CeO_2 and decreased in Ru(NC)/CeO_2 (Figure 4d and Table S2), demonstrating the reaction-induced enhancement and reduction of chemical interactions for Ru(SA)/CeO_2 and Ru(NC)/CeO_2, respectively.

The XPS characterizations gave results that were somewhat different from Raman observations. From Figure S7, a certain amount of Ce^{3+} ions was present on the surface of Ru(NC)/CeO_2 while the surface Ce^{3+} ions in Ru(SA)/CeO_2 and Ru(NP)/CeO_2 cannot even be detected. This phenomenon may be caused by the ex situ measurements of the reduced and reacted samples, since it has been proved that the uptake of O_2 by CeO_2 can take place at room temperature.[58] The O_2 in the air readily altered the surface electronic states measured from XPS characterization, while the oxygen vacancies from Raman spectroscopy were generated via the relocation of oxygen anions[56] and were hardly affected by the O_2 molecules at room temperature. The valences of Ru species from XPS, on the other hand, were also insensitive to the O_2 at room temperature, as can be inferred from the O_2-TPD and TPO profiles of the supported Ru species.[59,60]

Thus, the XPS peaks of Ru 3d were deconvoluted to analyze the Ru species in different oxidation states,[15,61,62] which were mainly composed of Ru(III) from $RuCl_3$, Ru(IV) from RuO_2, and Ru(VI) from RuO_3, with the average Ru valences decreasing from +4.1 in Ru(SA)/CeO_2 to +3.7 in Ru(NP)/CeO_2 on reduction by H_2 (Figure 5 and Table S3). Considering that the overlap between the C 1s and Ru 3d peaks makes the results dependent on the deconvolution, the Ru 3p profiles were also analyzed to provide additional evidence.[63,64] It turned out that Ru valences also decreased slightly (Figure 5 and Table S3), though some differences in specific values were present due to the different intensities of Ru 3d and Ru 3p XPS signals. Because the charge density of Ru deposits is merely affected by the interfacial charge transfer, their oxidation states are immediately correlated with the strength of electronic interaction of SMSI, exhibiting a reduced electronic interaction from Ru single atoms to nanoparticles. The average valence of Ru deposits increased slightly in Ru(SA)/CeO_2 and decreased in Ru(NC)/CeO_2, implying the respective reaction-induced enhancement and reduction of electronic interaction for these two samples, just like the aforementioned variation of the chemical counterpart indicated by Raman intensities.

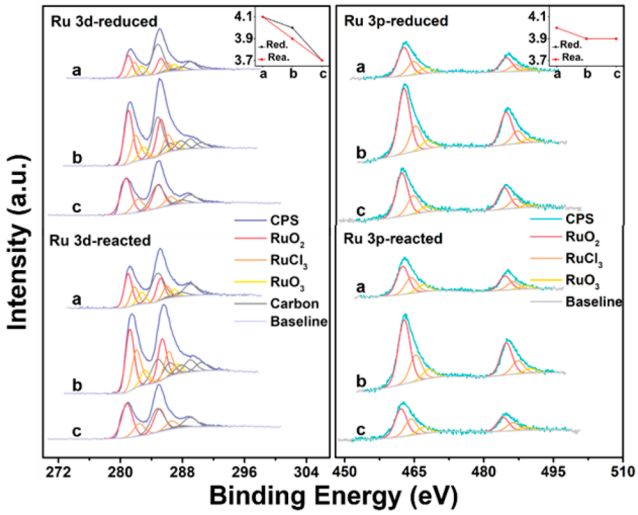

Figure 5. XPS spectra and peak fitting curves of (a) Ru(SA)/CeO_2, (b) Ru(NC)/CeO_2, and (c) Ru(NP)/CeO_2 after H_2 reduction and CO_2 methanation. The inset panels are the calculated average Ru valences for the reduced (Red.) and reacted (Rea.) catalysts calculated from Ru 3d and Ru 3p XPS profiles, respectively.

In general, the combined Raman and XPS analyses reveal the decreasing SMSI from Ru(SA)/CeO_2 to Ru(NP)/CeO_2, whether the electronic interactions of interfacial charge transfer from Ru deposits to CeO_2 supports or the chemical interactions arising from the density of interfacial bonding occur. In the methanation process, the SMSIs in Ru(SA)/CeO_2 and Ru(NC)/CeO_2 were respectively enhanced and reduced.

The H-spillover effect was examined by H_2-TPR and H_2-TPD measurements. In the reduction process, it can be observed that there were three main peaks centered at 140−170 °C (peak I), 220−280 °C (peak II), and around 430 °C (peak III) (Figure 6), which are attributed to the RuO_x species

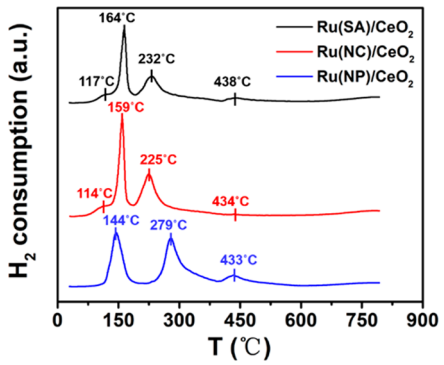

Figure 6. H_2-TPR profiles of Ru(SA)/CeO_2, Ru(NC)/CeO_2, and Ru(NP)/CeO_2.

strongly interacting with CeO_2 supports, the weakly interacting RuO_x species, and the surface and subsurface oxygens on CeO_2,[15] respectively. There was also a shoulder peak at 114 or 117 °C caused by the oxygen adsorption (Figure 6).[57] The reduction temperature of peak I was gradually lowered from 164 °C in Ru(SA)/CeO_2 to 144 °C in Ru(NP)/CeO_2, not in line with the variation of the SMSI or the oxidation states of the RuO_x species in these systems. H-spillover effects at Ru sites have been reasoned to improve the reducibility under an H_2 atmosphere,[65] and in our observations, the H-spillover effects

DOI: 10.1021/acscatal.7b04469
ACS Catal. 2018, 8, 6203−6215

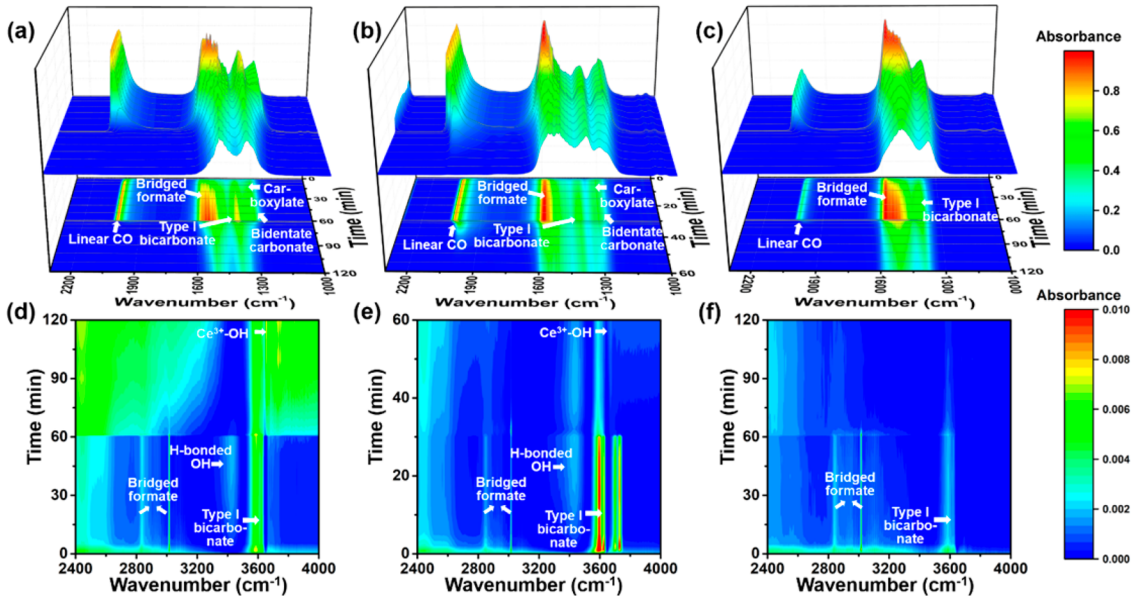

Figure 7. In situ DRIFTS results of (a, d) Ru(SA)/CeO_2, (b, e) Ru(NC)/CeO_2, and (c, f) Ru(NP)/CeO_2 from 2300 to 1000 cm^{-1} and from 4000 cm^{-1} to 2400 cm^{-1}, with the atmosphere switched from 1% CO_2/4% H_2/He to 5% H_2/He after stabilization at 220 °C for 60 min for Ru(SA)/CeO_2 and Ru(NP)/CeO_2 and 30 min for Ru(NC)/CeO_2. Before the measurement, the samples were pretreated at 300 °C for 30 min under 40 mL/min 5% H_2/He. The spectra are normalized respectively to compare the relative variation of surface species, and the characteristic signals of the active species are marked in the pictures.

also occurred to modify the reduction processes. Peak I also contains the H-spillover effect in which the H atoms chemically adsorbed on the RuO_x species are transported to the surfaces. Ru(NP)/CeO_2 has the strongest H-spillover capability and thus the lowest temperature of peak I. For peak II, however, the temperature decreased within 10 °C from Ru(SA)/CeO_2 to Ru(NC)/CeO_2 but was elevated nearly 50 °C for Ru(NP)/CeO_2, where the H-spillover no longer masked the effect of SMSI due to the large proportion of weakly interacting RuO_x species in Ru(NP)/CeO_2. The weakest interaction in the interface accounted for the high temperature of peak II. Moreover, the intensity ratio of peak II to peak I grew monotonously along with the variation from single atoms to large particles and was close to 1 for Ru(NP)/CeO_2, manifesting the increasing proportion of weakly interacting RuO_x species. On the whole, it emerges from the combined measurements that the H-spillover effects display contrasting tendencies toward the SMSI from Ru(SA)/CeO_2 to Ru(NP)/CeO_2, which can be reasonably understood from the competition between Ru−H bond strength and Ru−O−Ce charge transfer at one Ru site.

More quantitatively, the amount of spilled hydrogens was determined by an H_2-TPD experiment (Figure S8). The desorption peaks centered at 41, 75, and 90 °C are attributed to the hydrogens adsorbed on the Ru species, and the broad peaks from 350 to 720 °C are those adsorbed on the CeO_2 supports as well as those spilled from the Ru sites to the supports.[66] The H_2/M ratios of the Ru deposits and CeO_2 supports were calculated from the areas of the corresponding desorption peaks (Table S4). It can be seen that the H_2/Ru ratio decreased sharply from 0.61 to 0.16 in Ru(SA)/CeO_2 and Ru(NC)/CeO_2, accompanied by the increased H_2/ceria ratio from 0.03 to 0.06, suggesting the observable H-spillover effects in Ru(NC)/CeO_2. From Ru(NC)/CeO_2 to Ru(NP)/CeO_2, the H_2/Ru ratio further decreased to 0.14, although the H_2/ceria ratio also seemed slightly decreased. In combination with the results of H_2-TPR, the H-spillover effect was gradually augmented from Ru(SA)/CeO_2 to Ru(NC)/CeO_2 and Ru(NP)/CeO_2.

3.3. Reaction Pathways Dominated by the Activation of Metal Carbonyls and the Removal of H_2O Molecules.

With the knowledge of the predominant interfacial effects in the Ru/CeO_2 methanation catalysts, the influences exerted by the interfacial effects on the methanation activities were systematically surveyed via in situ DRIFTS measurements. The assignments of IR bands generally include three parts: that is, OH band, CO band, and formate and carbonate band (Table S5).[67−80] The type I, type II, and type III OH refer to the terminal, bridged, and triply bridged hydroxyls, respectively. Type I and type II bicarbonates refer to those coordinated with the oxygen atom of hydroxyls and the other oxygen atom, respectively. To distinguish the active species in the reaction, the atmosphere was switched from reaction gases to H_2, with the active species vanishing rapidly (Figure 7 and Figures S9−S11). For Ru(SA)/CeO_2, the surface species under a reactive atmosphere were bidentate carbonates (1559, 1288 cm^{-1}), polydentate carbonates (1480−1450, 1396 cm^{-1}), inorganic carboxylates (1559, 1508, 1305 cm^{-1}), and a few bicarbonates (3623, 1396, 1048 cm^{-1}), with the bridged formates (3017, 2836, 1580, 1339 cm^{-1}) and formyl groups (1765 cm^{-1}) occurring later on (Figure 7a,d and Figure S9). When the gases were switched to H_2, the bands of type I bicarbonates, bidentate carbonates, bridged formates, formyl groups, and inorganic carboxylates obviously weakened while the others stayed unchanged. Thus, the former are the active species. The OH bands offer information on surface hydroxylation. The structure of Ce^{3+}−OH (3653 cm^{-1}) immediately disappeared within 1 min in the reaction flow (Figure S9b), and type I bicarbonates (3623 cm^{-1}) and type III OH (3590, 3583 cm^{-1}) were formed (Figure 7d and Figure S9b). Following the reaction the intensity of H-bonded OH band (3426 cm^{-1}) gradually increased to a stabilized value, indicating the formation of a

DOI: 10.1021/acscatal.7b04469
ACS Catal. 2018, 8, 6203−6215

network of H bonds. Under an H_2 atmosphere (Figure 7d and Figure S9b), the bicarbonates were quickly converted to bridged formates (3017 cm^{-1}), which decreased afterward, along with the complete consumption of H-bonded OH. Finally, the structure of Ce^{3+}−OH appeared again (Figure S9b), accompanied by the increase of type I and II OH.

The reaction pathways of Ru(NC)/CeO_2 included the additional transformation from bridged formates (3016, 2848, 1542, 1327 cm^{-1}) to bridged carbonates (1191 cm^{-1}) (Figure S10a), and the proportion of formates was evidently reduced (Figure 7b), in comparison to that of Ru(SA)/CeO_2. Under the reaction atmosphere, type I OH (3728 cm^{-1}) and H-bonded OH (3436 cm^{-1}) increased simultaneously (Figure 7e and Figure S10b), representative of the surface that was partially covered by the H bond network with the other sites terminated by type I OH. On exposure to an H_2 atmosphere, the H bond network (3436 cm^{-1}) remained unreduced (Figure 7e and Figure S10b). Meanwhile, type I (3728 cm^{-1}) and type III OH (3594 cm^{-1}) species disappeared with a small amount of type II OH (3672 cm^{-1}) appearing (Figure S10b).

For Ru(NP)/CeO_2, the pathway from bridged formates (3017, 2841, 1540, 1340 cm^{-1}) to bidentate carbonates was missing, and polydentate carbonates still acted as spectators in the reaction (Figure 7c and Figure S11). Different from the above two catalysts, H-bonded OH groups (3456 cm^{-1}) were slightly formed only after the gas flow was switched to H_2, and almost no Ce^{3+}−OH sites were regenerated (Figure S11b).

In addition, the active sites of the methanation catalysts were verified via steady-state DRIFTS experiments, where the catalysts were stabilized under the reactive atmosphere for 1 h from 50 to 300 °C (Figure S12). The band at 2847−2852 cm^{-1}, attributed to the bridged formate on CeO_2[76,80] disappeared at 200 °C. Another band at 3016 cm^{-1} appeared and grew stronger from 200 to 300 °C. The latter is attributed to the bridged formate adsorbed at the interface of the Ru deposits and the CeO_2 supports, and the electrons donated by the Ru deposits to the Ce sites enhanced the stretching vibration of the C−H bond in the bridge formate, giving rise to the shift from 2847−2852 to 3016−3017 cm^{-1}. In combination with the observations that E_a varied greatly with the size of Ru deposits and that Ce^{3+}−OH was immediately reacted after switching from CO_2/H_2/He to H_2/He, the specific active sites were the Ce^{3+}−OH sites and Ru sites at the interface.

The conversion mechanism from adsorbed CO_2 to metal carbonyls deduced from DRIFTS results is summarized in Figure S13 and paths I−III, where the CO_2-derived type I bicarbonates are converted to bridged formates (path I), bidentate or bridged carbonates (path II), and inorganic carboxylates (path III) and then to Ru carbonyls. In the following equations, O_L denotes lattice oxygen atoms and asterisks denote the sites on the surfaces.

$$CO_2 + Ce^{3+}\text{−OH} \rightarrow HCO_3\text{−}Ce^{3+} \quad \text{(I-1)}$$

$$HCO_3\text{−}Ce^{3+} \rightarrow HCO_2\text{−}Ce^{4+} + O_L \quad \text{(I-2)}$$

$$HCO_2\text{−}Ce^{4+} \rightarrow CO_2\text{−}Ce^{4+} + H^* \quad \text{(I-3)}$$

$$CO_2\text{−}Ce^{4+} + H^* + Ru \rightarrow Ru\text{−}CO + Ce^{4+}\text{−OH} + * \quad \text{(I-4)}$$

$$CO_2 + Ce^{3+}\text{−OH} \rightarrow HCO_3\text{−}Ce^{3+} \quad \text{(II-1)}$$

$$HCO_3\text{−}Ce^{3+} + * \rightarrow CO_3\text{−}Ce^{3+} + H^* \quad \text{(II-2)}$$

$$CO_3\text{−}Ce^{3+} + H^* + Ru \rightarrow Ru\text{−}CO + Ce^{4+}\text{−OH} + O_L + * \quad \text{(II-3)}$$

$$CO_2 + Ce^{3+}\text{−OH} \rightarrow O_2C\text{−}Ce^{3+}\text{−OH} \quad \text{(III-1)}$$

$$O_2C\text{−}Ce^{3+}\text{−OH} + Ru \rightarrow Ru\text{−}CO + Ce^{4+}\text{−OH} + O_L \quad \text{(III-2)}$$

The Ru carbonyls are activated by chemisorbed H atoms, and formyl groups are generated, which are finally converted to CH_4 molecules. The overall methanation process is in line with the CO route that has been extensively discussed in the literature.[23,24,81] Another possibility of the direct hydrogenation of bridged formates to produce CH_4 is not excluded, but it cannot be the major route because the characteristic band of methanol at 1008 cm^{-1} was not detectable in our measurements.[82] In the CO route, the activation of metal carbonyls is always identified as the rate-determining step.[81] Nevertheless, the removal of the residual oxygen atom in CO_2 by H atoms to keep the mass balance of the methanation reaction (Figure S13), that is, the removal of H_2O molecules via the combination of H atoms and OH groups on the surfaces, is also quite important, and the step has been proved by kinetic modeling to be irreversible.[23] This irreversible step after the rate-determining step is able to strongly affect the reaction rate as well. Thereby, the key elementary steps governing the methanation activity are

$$Ru\text{−}CO + H^* \rightarrow Ru\text{−}CHO + * \quad \text{(i)}$$

$$H^* + {}^*OH \rightarrow H_2O^* + * \quad \text{(ii)}$$

$$H_2O^* \rightarrow H_2O + * \quad \text{(iii)}$$

Accordingly, the carbon-containing species that was discovered to greatly hinder the methanation process in the kinetic measurements is likely to be metal carbonyl. Not only are the carbonyls the most difficult to activate but also each consumes one oxygen vacancy with the O atom left from the adsorbed CO_2 molecules.[83] The oxygen vacancy provides the active site of Ce^{3+}−OH in charge of CO_2 dissociation, while the other active site, i.e. the Ru site, hydrogenates the metal carbonyl synergistically.

The behavior of OH groups on the surface is closely affiliated with H_2O removal from the catalysts. As indicated by the OH bands in DRIFTS measurements, after a switch to an H_2 atmosphere, the H-bonded OH disappeared in Ru(SA)/CeO_2 (Figure 7d and Figure S9) but remained unchanged in Ru(NC)/CeO_2 (Figure 7e and Figure S10) and was slightly generated in Ru(NP)/CeO_2 (Figure S11). Thus, H-bonded OH was able to actively participate in the methanation process, and the observable H-spillover effects in Ru(NC)/CeO_2 and Ru(NP)/CeO_2 were again verified, in which the H-spillover effect contributed to the compensation and generation of H-bonded OH,[84] respectively. On the other hand, the regeneration of Ce^{3+}−OH sites under an H_2 atmosphere weakened from Ru(SA)/CeO_2 to Ru(NP)/CeO_2 (Figure 7d−f and Figures S9−S11). On exposure to the reactive atmosphere, the active sites of Ce^{3+}−OH disappeared right away (Figures S9b−S11b) because the oxygen vacancies next to the Ce^{3+}−OH sites were eliminated by the oxygen atoms dissociated from CO_2 molecules, and their regeneration under H_2 atmosphere

DOI: 10.1021/acscatal.7b04469
ACS Catal. 2018, 8, 6203−6215

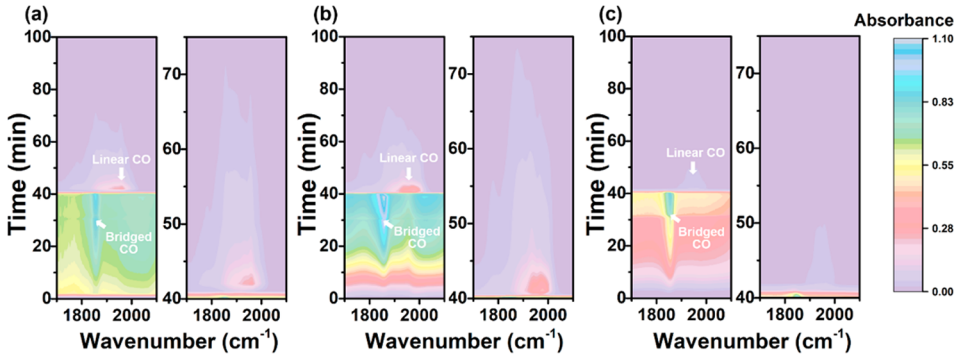

Figure 8. In situ DRIFTS results of (a) Ru(SA)/CeO_2, (b) Ru(NC)/CeO_2, and (c) Ru(NP)/CeO_2 from 2100 to 1700 cm^{-1}, along with the gas switchover from CO_2 to H_2. Before the measurement, the samples were pretreated at 300 °C for 30 min under 40 mL/min 5% H_2/He. In the experiment, 40 mL/min 5% CO_2/He was introduced into the DRIFTS cell at 220 °C for 30 min, after which He was used to purge the cell for 10 min, and then the atmosphere was switched to 5% H_2/He and stabilized for 60 min. The DRIFTS spectra right after the introduction of H_2 in the left panel are magnified and shown as the right panel.

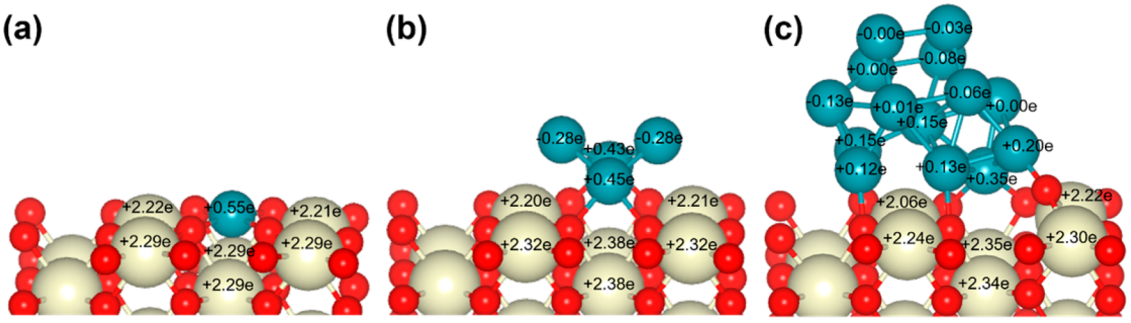

Figure 9. Bader charge analyses of the original (a) Ru_1/CeO_2, (b) Ru_4/CeO_2, and (c) Ru_{14}/CeO_2 in a front view. Ru (blue spheres), Ce (yellow spheres), O (red spheres), and C (brown spheres) atoms are shown.

arose (Figure 7d–f and Figures S9b–S11b and S13) due to the removal of H_2O molecules. Therefore, the removal of H_2O molecules is thought to decrease from Ru(SA)/CeO_2 to Ru(NP)/CeO_2, with the simultaneous enhancement of H-spillover effect.

To analyze the ability of the three catalysts to activate carbonyls in the reaction, transient DRIFTS measurements after a switch from a CO_2 atmosphere to an H_2 atmosphere were conducted on the three catalysts. CO_2 instead of the reaction atmosphere guarantees that the carbonyls derived from CO_2 are all preserved and later activated by chemisorbed H atoms. The activation ability could be compared from the extinction speeds of the CO band at 2000–1800 cm^{-1} (Figure 8 and Figure S14). The strongest CO band emerging in the CO_2/He atmosphere was located at around 1850 cm^{-1} (Figure 8), a quite low wavenumber in comparison to that in the former DRIFTS experiment. This is because the dissociation of CO_2 molecules without H assistance under the experimental conditions is relatively slowed and the small quantity of carbonyls was attached to Ru sites in bridged forms. On introduction of H_2, all of the CO bands rapidly dropped to a rather low intensity within 1 min (Figure S14), and the CO band at around 1950 cm^{-1} (Figure 8) was left over, which was attributed to the linearly adsorbed carbonyls. Therefore, the bridged carbonyls are much more active than the linearly adsorbed carbonyls. The latter, however, were mainly observed under the reaction atmosphere; therefore, the hydrogenation of the latter carbonyls determines the general activation ability of Ru carbonyls to a great extent. On comparison of the extinction of the linearly adsorbed CO bands for the three catalysts, the band on Ru(NP)/CeO_2 was the fastest to become extinct, and those on the other two catalysts were similar to each other in extinction rate. In combination with the extinction speeds of bridged CO bands, the activation ability of Ru carbonyls follows the sequence Ru(SA)/CeO_2 < Ru(NC)/CeO_2 < Ru(NP)/CeO_2. In addition, the constant frequency of the Ru–CO band during CO_2 adsorption (Figure 8) also certifies that CO_2 molecules are mainly adsorbed on the CeO_2 supports, not on the Ru deposits, for their dissociative adsorption on the Ru deposits would cause a change in Ru valences and shift in Ru–CO bands.

3.4. Competition of SMSI and H-Spillover Effect in Determining the Methanation Activity. With regard to the mechanistic understanding of the internal causes of the carbonyl activation and H_2O removal in determining the methanation activities, first-principles DFT calculations were carried out on the basis of the models of Ru_1, Ru_4, and Ru_{14} supported on the CeO_2(110) slabs. Though the sizes of the models and the samples varied to some extent, the variations of the two effects were both monotonous with the metal size experimentally, which ensures that the calculations based on current models are indicative of the practical catalysts.[39,42] The Ru deposits with certain amounts of Ru–O coordination were charged positively, which we ascribed to the strong interaction between the Ru deposits and the oxygen atoms in the Ru–CeO_2 interface,[31,42,85] with no consideration of oxygen atoms on top of the deposits. Bader charge analyses of the three models proved the correlation between the SMSI and the carbonyl activation on the Ru deposits. The most intense SMSI of Ru_1/CeO_2 was disclosed by the most positive charge, +0.55 e

DOI: 10.1021/acscatal.7b04469
ACS Catal. 2018, 8, 6203–6215

on the Ru atom, and the least positive average charge was found for Ce atoms next to the Ru deposits (Figure 9). Correspondingly, the CO adsorbed on Ru_1/CeO_2 had the most positively charged C atom (+0.85 e) (Figure S15a–c) and the least binding energy (−153 kJ mol^{-1}) (Table S6), which is not advantageous to CO activation. The CO molecules on Ru_4/CeO_2 and Ru_{14}/CeO_2, however, gained more electrons from the Ru deposits and were moderately stabilized by the adsorption configuration, on which the activation of the C═O bond would be largely facilitated. Thus, the electrons donated from the Ru deposits to the adsorbed CO molecules increase from highly oxidized single atoms to largely reduced nanoparticles, which leads to the improved carbonyl activation.

On the other hand, the H-spillover effect was found to greatly affect the removal of H_2O molecules. The H-spillover process is closely related to the H coverage on the surface.[86] To approximate the real process as much as possible, the number of H atoms residing on the Ru deposits in the final states of spillover were estimated according to the H_2/Ru ratio from H_2-TPD experiments, which gave n(H) values on Ru_1/CeO_2, Ru_4/CeO_2, and Ru_{14}/CeO_2 of 1.22, 1.28, and 3.92, respectively. Thus, one H atom was placed on Ru_1 and Ru_4, while four H atoms were placed on Ru_{14} in the final state. The H-spillover process was designed to start from H_2 dissociation to chemisorbed H atoms ($*H_{Ru}$), with one H atom diffusing to the interface ($*H_{int}$) and finally to the neighboring ceria sites ($*H_{ceria}$) to form surface hydroxyls (Figure 10). The spillover

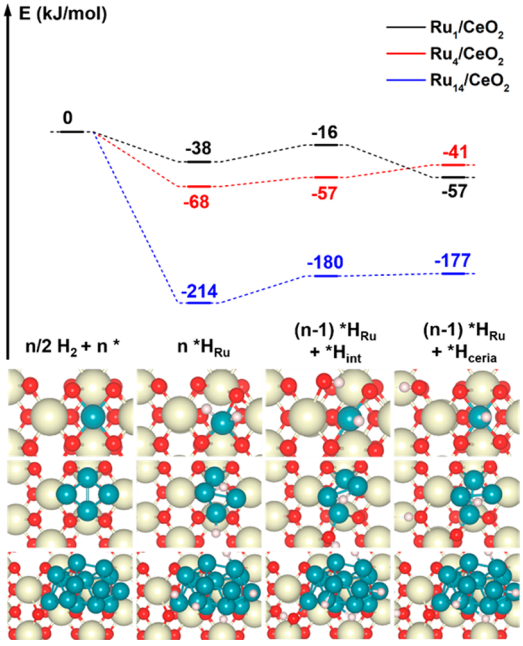

Figure 10. Energy profiles and corresponding structures in the process of H-spillover on Ru_1/CeO_2 (black line and the first row), Ru_4/CeO_2 (red line and the second row), and Ru_{14}/CeO_2 (blue line and the third row) in a top view. Ru (blue spheres), Ce (yellow spheres), O (red spheres), and H (pink spheres) atoms are shown.

energetics of Ru_{14}/CeO_2 was the most favored due to the evident stabilization effect of H_2 chemisorption, and its energy was 146 kJ mol^{-1} lower than that of Ru_4/CeO_2 and 176 kJ mol^{-1} lower than that of Ru_1/CeO_2. The stabilization effect is explained by the abundant electrons donated by larger Ru deposits to the H_2 molecules, as can be seen from the Bader charge analyses of the model catalysts (Figure S16a,c,e). The average valences of $*H_{Ru}$ atoms in Ru_1/CeO_2, Ru_4/CeO_2, and Ru_{14}/CeO_2 were −0.16, −0.20, and −0.28 e, respectively. It is reasonably speculated that the excess electrons from Ru_{14} fill the antibonding orbitals of the H_2 molecules and that H_2 chemisorption is largely facilitated and stabilized. For the effect of H-spillover on H_2O removal, the densities of states (DOSs) projected on the $*H_{Ru}$ atoms that were ready for the next spillover were compared (Figure S16b,d,f). The 1s orbitals of the $*H_{Ru}$ atoms entirely shifted to lower energies and away from the Fermi level from Ru_1/CeO_2 to Ru_4/CeO_2 and Ru_{14}/CeO_2, indicating the decreasing reactivities of the $*H_{Ru}$ atoms,[87] which finally give rise to the weakened H_2O removal.[88,89]

Hence, the SMSI and H-spillover effects are augmented respectively in CeO_2-supported single Ru atoms and large Ru nanoparticles, and the two effects respectively affect the activation of metal carbonyls and the dehydration of the surfaces in the opposite directions, exerting a combining influence on the methanation activities (Scheme 1). Only when the two effects achieve a balance, as was the case in Ru(NC)/CeO_2, could the methanation activity be promoted to the optimal value.

Scheme 1. Competitive SMSI and H-Spillover Effect Lead to Competing CO Activation and Surface Dehydration for CeO_2-Supported Single Ru Atoms, Ru Nanoclusters, and Large Ru Nanoparticles

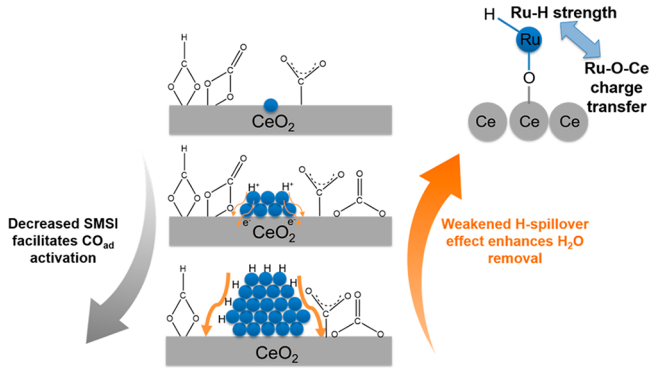

4. CONCLUSIONS

The interfacial effects of CO_2 methanation on highly active Ru/CeO_2 catalysts in different size regimes were systematically investigated, among which the SMSI and H-spillover effects were demonstrated to competitively determine the methanation activities. In comparison with the activity change caused by the nonequivalent doping of CeO_2 supports, that due to the variation of Ru size regimes is more notable, demonstrating that the rate-determining step takes place on the Ru deposits rather than the surfaces of the supports. The TOFs of CeO_2-supported single Ru atoms, Ru nanoclusters, and Ru nanoparticles at 190 °C are 4.59×10^{-3}, 7.41×10^{-3}, and 5.30×10^{-4} s^{-1}, respectively, with 100% CH_4 selectivity. On the other hand, the negative CO_2 reaction orders decrease in absolute values and turn positive from supported single Ru atoms to nanoparticles, while the positive H_2 reaction orders increase, which demonstrates the gradually eliminated hindrance of CO_2-derived intermediates and the weighted dependence on H_2 partial pressure. The spectroscopic experiments provided mechanistic insights into the interfacial effects leading to the

DOI: 10.1021/acscatal.7b04469
ACS Catal. 2018, 8, 6203–6215

activity differences. Above all, the dominant reaction pathway is the CO route, where the metal carbonyls are the critical intermediates and the active sites are Ce^{3+}−OH sites and Ru sites near the metal−support interfaces responsible for CO_2 dissociation and carbonyl hydrogenation, respectively. The SMSI is the strongest for CeO_2 -supported single Ru atoms, regardless of the electronic interaction of charge transfer via Ru−O−Ce or the chemical interactions arising from the density of interfacial bonding. Among them, the electronic interaction evidently alters the activation ability of metal carbonyls, the rate-determining step in CO routes, and strong interfacial charge transfer is disadvantageous for carbonyl activation. In addition, H-spillover effects are present in both CeO_2-supported Ru nanoclusters and nanoparticles in the reaction, with the intensity much more enhanced in the latter assembly, where the removal of H_2O molecules is greatly hindered. The SMSI and H-spillover effects are actually in a competitive relationship, just as there is competition between Ru−H bond strength and charge transfer via Ru−O−Ce. The two factors lead to the reverse variations of metal carbonyl activation and H-spillover effects for the methanation catalysts in different size regimes, which are balanced at CeO_2-supported Ru nanoclusters to exhibit superior low-temperature methanation activity. This work illuminates the significant catalytic activity differences in the extended size regimes, which notably broadens the horizon in engineering high-performance supported metal catalysts applied in a broad scope of heterogeneous catalytic reactions from the perspective of size sensitivity and intrinsically tunable interfacial effects between metal and supports.

■ ASSOCIATED CONTENT

Supporting Information

The Supporting Information is available free of charge on the ACS Publications website at DOI: 10.1021/acscatal.7b04469.

EXAFS fitting results, oxygen vacancies in CeO_2 supports from Raman sepctra, valence states of surface species from XPS results, H_2/M ratios from H_2-TPD, assignment of IR bands, CO binding energies from DFT calculations, TEM and HRTEM images of the fresh and spent catalysts, EXAFS curves, methanation reactivity plots, DRIFTS spectra, reaction pathways from CO_2 to CH_4 and CO, Bader charge analyses of CO activation and H-spillover, and projected density of states of the adsorbed H atoms in the H-spillover process (PDF)

■ AUTHOR INFORMATION

Corresponding Authors

*E-mail for H.-C.L.: hcliu@pku.edu.cn.
*E-mail for Y.-W.Z.: ywzhang@pku.edu.cn.

ORCID

Hai-Chao Liu: 0000-0001-9175-3371
Chun-Hua Yan: 0000-0002-0581-2951
Ya-Wen Zhang: 0000-0002-1871-7507

Notes

The authors declare no competing financial interest.

■ ACKNOWLEDGMENTS

This work was supported by the National Key Research and Development Program of the MOST of China (No. 2016YFB0701100), the Natural Science Foundation of China (No. 21573005, 21771009, and 21621061), the Beijing Natural Science Foundation (No. 2162019), and the project funded by Jiangsu Key Laboratory of Vehicle Emissions Control (No. OVEC016). The computational work was supported by the High-performance Computing Platform of Peking University. We particularly appreciate the help of Dr. Wei-Zhen Li and Mr. Xian-Rui Gu in the XAFS and DRIFTS measurements, respectively. We also thank the Electron Microscopy Laboratory of Peking University for the cs-corrected HAADF-STEM observations.

■ REFERENCES

(1) Centi, G.; Perathoner, S. CO_2-Based Energy Vectors for the Storage of Solar Energy. Greenh. *Greenhouse Gases: Sci. Technol.* **2011**, *1*, 21−35.
(2) Zhang, X.; Li, X.; Zhang, D.; Su, N. Q.; Yang, W.; Everitt, H. O.; Liu, J. Product Selectivity in Plasmonic Photocatalysis for Carbon Dioxide Hydrogenation. *Nat. Commun.* **2017**, *8*, 14542.
(3) Rao, H.; Schmidt, L. C.; Bonin, J.; Robert, M. Visible-Light-Driven Methane Formation from CO_2 with a Molecular Iron Catalyst. *Nature* **2017**, *548*, 74−77.
(4) Sung, S.; Kumar, D.; Gil-Sepulcre, M.; Nippe, M. Electrocatalytic CO_2 Reductoin by Imidazolium-Functionalized Molecular Catalysts. *J. Am. Chem. Soc.* **2017**, *139*, 13993−13996.
(5) Wang, W.; Wang, S.; Ma, X.; Gong, J. Recent Advances in Catalytic Hydrogenation of Carbon Dioxide. *Chem. Soc. Rev.* **2011**, *40*, 3703−3727.
(6) Kattel, S.; Liu, P.; Chen, J. G. Tuning Selectivity of CO_2 Hydrogenation Reactions at the Metal/Oxide Interface. *J. Am. Chem. Soc.* **2017**, *139*, 9739−9754.
(7) Rönsch, S.; Schneider, J.; Matthischke, S.; Schlüter, M.; Götz, M.; Lefebvre, J.; Prabhakaran, P.; Bajohr, S. Review on Methanation − From Fundamentals to Current Projects. *Fuel* **2016**, *166*, 276−296.
(8) Aziz, M. A. A.; Jalil, A. A.; Triwahyono, S.; Ahmad, A. CO_2 Methanation over Heterogeneous Catalysts: Recent Progress and Future Prospects. *Green Chem.* **2015**, *17*, 2647−2663.
(9) Jia, J.; Qian, C.; Dong, Y.; Li, Y. F.; Wang, H.; Ghoussoub, M.; Butler, K. T.; Walsh, A.; Ozin, G. A. Heterogeneous Catalytic Hydrogenation of CO_2 by Metal Oxides: Defect Engineering − Perfecting Imperfection. *Chem. Soc. Rev.* **2017**, *46*, 4631−4644.
(10) Liu, C.; Yang, B.; Tyo, E.; Seifert, S.; DeBartolo, J.; von Issendorff, B.; Zapol, P.; Vajda, S.; Curtiss, L. A. Carbon Dioxide Conversion to Methanol over Size-Selected Cu_4 Clusters at Low Pressures. *J. Am. Chem. Soc.* **2015**, *137*, 8676−9.
(11) Wu, C.; Zhang, Z.; Zhu, Q.; Han, H.; Yang, Y.; Han, B. Highly Efficient Hydrogenation of Carbon Dioxide to Methyl Formate over Supported Gold Catalysts. *Green Chem.* **2015**, *17*, 1467−1472.
(12) Cargnello, M.; Doan-Nguyen, V.; Gordon, T. R.; Diaz, R. E.; Stach, E. A.; Gorte, R. J.; Fornasiero, P.; Murray, C. B. Control of Metal Nanocrystal Size Reveals Metal-Support Interface Role for Ceria Catalysts. *Science* **2013**, *341*, 771−773.
(13) Mutz, B.; Belimov, M.; Wang, W.; Sprenger, P.; Serrer, M.-A.; Wang, D.; Pfeifer, P.; Kleist, W.; Grunwaldt, J.-D. Potential of an Alumina-Supported Ni_3Fe Catalyst in the Methanation of CO_2: Impact of Alloy Formation on Activity and Stability. *ACS Catal.* **2017**, *7*, 6802−6814.
(14) Tada, S.; Ochieng, O. J.; Kikuchi, R.; Haneda, T.; Kameyama, H. Promotion of CO_2 Methanation activity and CH4 Selectivity at Low Temperatures over $Ru/CeO_2/Al_2O_3$ catalysts. *Int. J. Hydrogen Energy* **2014**, *39*, 10090−10100.
(15) Wang, F.; Li, C.; Zhang, X.; Wei, M.; Evans, D. G.; Duan, X. Catalytic Behavior of Supported Ru Nanoparticles on the {100}, {110}, and {111} Facet of CeO_2. *J. Catal.* **2015**, *329*, 177−186.
(16) Larmier, K.; Liao, W. C.; Tada, S.; Lam, E.; Verel, R.; Bansode, A.; Urakawa, A.; Comas-Vives, A.; Coperet, C. CO_2-to-Methanol Hydrogenation on Zirconia-Supported Copper Nanoparticles: Reaction Intermediates and the Role of the Metal-Support Interface. *Angew. Chem., Int. Ed.* **2017**, *56*, 2318−2323.

DOI: 10.1021/acscatal.7b04469
ACS Catal. 2018, 8, 6203−6215

(17) Kattel, S.; Yu, W.; Yang, X.; Yan, B.; Huang, Y.; Wan, W.; Liu, P.; Chen, J. G. CO_2 Hydrogenation over Oxide-Supported PtCo Catalysts: The Role of the Oxide Support in Determining the Product Selectivity. *Angew. Chem., Int. Ed.* **2016**, *55*, 7968−7973.
(18) Zhan, G.; Zeng, H. C. ZIF-67-Derived Nanoreactors for Controlling Product Selectivity in CO_2 Hydrogenation. *ACS Catal.* **2017**, *7*, 7509−7519.
(19) Karelovic, A.; Ruiz, P. CO_2 Hydrogenation at Low Temperature over Rh/γ-Al_2O_3 Catalysts: Effect of the Metal Particle Size on Catalytic Performances and Reaction Mechanism. *Appl. Catal., B* **2012**, *113*−*114*, 237−249.
(20) Karelovic, A.; Ruiz, P. Mechanistic Study of Low Temperature CO_2 Methanation over Rh/TiO_2 Catalysts. *J. Catal.* **2013**, *301*, 141−153.
(21) Abe, T.; Tanizawa, M.; Watanabe, K.; Taguchi, A. CO_2 Methanation Property of Ru Nanoparticle-Loaded TiO_2 Prepared by a Polygonal Barrel-Sputtering Method. *Energy Environ. Sci.* **2009**, *2*, 315−321.
(22) Wang, X.; Shi, H.; Kwak, J. H.; Szanyi, J. Mechanism of CO_2 Hydrogenation on Pd/Al_2O_3 Catalysts: Kinetics and Transient DRIFTS-MS Studies. *ACS Catal.* **2015**, *5*, 6337−6349.
(23) Wang, X.; Hong, Y.; Shi, H.; Szanyi, J. Kinetic Modeling and Transient DRIFTS-MS Studies of CO_2 Methanation over Ru/Al_2O_3 Catalysts. *J. Catal.* **2016**, *343*, 185−195.
(24) Wang, X.; Shi, H.; Szanyi, J. Controlling Selectivities in CO_2 Reduction through Mechanistic Understanding. *Nat. Commun.* **2017**, *8*, 513.
(25) Liu, J. Catalysis by Supported Single Metal Atoms. *ACS Catal.* **2017**, *7*, 34−59.
(26) Qiao, B.; Wang, A.; Yang, X.; Allard, L. F.; Jiang, Z.; Cui, Y.; Liu, J.; Li, J.; Zhang, T. Single-Atom Catalysis of CO Oxidation Using Pt_1/FeO_x. *Nat. Chem.* **2011**, *3*, 634−641.
(27) Shan, J.; Li, M.; Allard, L. F.; Lee, S.; Flytzani-Stephanopoulos, M. Mile Oxidation of Methane to Methanol or Acetic Acid on Supported Isolated Rhodium Catalysts. *Nature* **2017**, *551*, 605−608.
(28) Guo, X.; Fang, G.; Li, G.; Ma, H.; Fan, H.; Yu, L.; Ma, C.; Wu, X.; Deng, D.; Wei, M.; Tan, D.; Si, R.; Zhang, S.; Li, J.; Sun, L.; Tang, Z.; Pan, X.; Bao, X. Direct, Nonoxidative Conversion of Methane to Ethylene, Aromatics, and Hydrogen. *Science* **2014**, *344*, 616−619.
(29) Van Santen, R. A. Complementary Structure Sensitive and Insensitive Catalytic Relationships. *Acc. Chem. Res.* **2009**, *42*, 57−66.
(30) Tyo, E. C.; Vajda, S. Catalysis by Clusters with Precise Numbers of Atoms. *Nat. Nanotechnol.* **2015**, *10*, 577−588.
(31) Vayssilov, G. N.; Lykhach, Y.; Migani, A.; Staudt, T.; Petrova, G. P.; Tsud, N.; Skala, T.; Bruix, A.; Illas, F.; Prince, K. C.; Matolin, V.; Neyman, K. M.; Libuda, J. Supported Nanostructure Boosts Oxygen Transfer to Catalytically Active Platinum Nanoparticles. *Nat. Mater.* **2011**, *10*, 310−315.
(32) Tauster, S. J.; Fung, S. C.; Garten, R. L. Strong Metal-Support Interactions. Group 8 Noble Metals Supported on Titanium Dioxide. *J. Am. Chem. Soc.* **1978**, *100*, 170−175.
(33) Tauster, S. J.; Fung, S. C. Strong Metal-Support Interactions: Occurrence among the Binary Oxides of Groups IIA-VB. *J. Catal.* **1978**, *55*, 29−35.
(34) Haller, G. L.; Resasco, D. E. Metal-Support Interaction: Group VIII Metals and Reducible Oxides. *Adv. Catal.* **1989**, *36*, 173−235.
(35) Schwab, G.-M. Electronics of Supported Catalysts. *Adv. Catal.* **1979**, *27*, 1−22.
(36) *Catalysis and Electrocatalysis at Nanoparticle Surfaces*; Wieckowski, A., Savinova, E. R., Vayenas, C. G., Eds.; CRC Press: Boca Raton, FL, 2003.
(37) Vernoux, P.; Lizarraga, L.; Tsampas, M. N.; Sapountzi, F. M.; Lucas-Consuegra, A. D.; Valverde, J.-L.; Souentie, S.; Vayenas, C. G.; Tsiplakides, D.; Balomenou, S.; Baranova, E. A. Ionically Conducting Ceramics as Active Catalyst Supports. *Chem. Rev.* **2013**, *113*, 8192−8260.
(38) Tauster, S. J.; Fung, S. C.; Baker, R. T. K.; Horsley, J. A. Strong Interactions in Supported-Metal Catalysts. *Science* **1981**, *211*, 1121−1125.
(39) Bruix, A.; Rodriguez, J. A.; Ramírez, P. J.; Senanayake, S. D.; Evans, J.; Park, J. B.; Stacchiola, D.; Liu, P.; Hrbek, J. Illas, Francesc. A New Type of Strong Metal-Support Interaction and the Production of H_2 through the Transformation of Water on Pt/CeO_2(111) and Pt/CeO_x/TiO_2(110) Catalysts. *J. Am. Chem. Soc.* **2012**, *134*, 8968−8974.
(40) Acerbi, N.; Edman Tsang, S. C.; Jones, G.; Golunski, S.; Collier, P. Rationalization of Interactions in Precious Metal/Ceria Catalysts Using the d-Band Center Model. *Angew. Chem., Int. Ed.* **2013**, *52*, 7737−7741.
(41) Willinger, M. G.; Zhang, W.; Bondarchuk, O.; Shaikhutdinov, S.; Freund, H.-J.; Schlögl, R. A Case of Strong Metal-Support Interactions: Combining Advanced Microscopy and Model Systems to Elucidate the Atomic Structure of Interfaces. *Angew. Chem., Int. Ed.* **2014**, *53*, 5998−6001.
(42) Ke, J.; Zhu, W.; Jiang, Y.; Si, R.; Wang, Y.-J.; Li, S.-C.; Jin, C.; Liu, H.; Song, W.-G.; Yan, C.-H.; Zhang, Y.-W. Strong Local Coordination Structure Effects on Subnanometer PtO_x Clusters over CeO_2 Nanowires Probed by Low-Temperature CO Oxidation. *ACS Catal.* **2015**, *5*, 5164−5173.
(43) Matsubu, J. C.; Zhang, S.; DeRita, L.; Marinkovic, N. S.; Chen, J. G.; Graham, G. W.; Pan, X.; Christopher, P. Adsorbate-Mediated Strong Metal-Support Interactions in Oxide-Supported Rh Catalysts. *Nat. Chem.* **2017**, *9*, 120−127.
(44) Ahmadi, M.; Mistry, H.; Roldan Cuenya, B. Tailoring the Catalytic Properties of Metal Nanoparticles via Support Interactions. *J. Phys. Chem. Lett.* **2016**, *7*, 3519−3533.
(45) Li, S.; Xu, Y.; Chen, Y.; Li, W.; Lin, L.; Li, M.; Deng, Y.; Wang, X.; Ge, B.; Yang, C.; Yao, S.; Xie, J.; Li, Y.; Liu, X.; Ma, D. Tuning the Selectivity of Catalytic Carbon Dioxide Hydrogenation over Iridium/Cerium Oxide Catalysts with a Strong Metal-Support Interaction. *Angew. Chem., Int. Ed.* **2017**, *56*, 10761−10765.
(46) Abdel-Mageed, A. M.; Widmann, D.; Olesen, S. E.; Chorkendorff, I.; Biskupek, J.; Behm, R. J. Selective CO Methanation on Ru/TiO_2 Catalysts: Role and Influence of Metal-Support Interactions. *ACS Catal.* **2015**, *5*, 6753−6763.
(47) Prins, R. Hydrogen Spillover: Facts and Fictions. *Chem. Rev.* **2012**, *112*, 2714−2738.
(48) Karim, W.; Spreafico, C.; Kleibert, A.; Gobrecht, J.; VandeVondele, J.; Ekinci, Y.; van Bokhoven, J. A. Catalyst Support Effects on Hydrogen Spillover. *Nature* **2017**, *541*, 68−71.
(49) Karelovic, A.; Ruiz, P. Improving the Hydrogenation Function of Pd/γ-Al_2O_3 Catalyst by Rh/γ-Al_2O_3 Addition in CO_2 Methanation at Low Temperature. *ACS Catal.* **2013**, *3*, 2799−2812.
(50) Beaumont, S. K.; Alayoglu, S.; Specht, C.; Michalak, W. D.; Pushkarev, V. V.; Guo, J.; Kruse, N.; Somorjai, G. A. Combining in situ NEXAFS Spectroscopy and CO_2 Methanation Kinetics to Study Pt and Co Nnanoparticle Catalysts Reveals Key Insights into the Role of Platinum in Promoted Cobalt Catalysis. *J. Am. Chem. Soc.* **2014**, *136*, 9898−9901.
(51) Ke, J.; Xiao, J. W.; Zhu, W.; Liu, H.; Si, R.; Zhang, Y. W.; Yan, C. H. Dopant-Induced Modification of Active Site Structure and Surface Bonding Mode for High-Performance Nanocatalysts: CO Oxidation on Capping-Free (110)-Oriented CeO_2:Ln (Ln = La-Lu). *J. Am. Chem. Soc.* **2013**, *135*, 15191−15200.
(52) Bergeret, G., Gallezot, P. In *Handbook of Heterogeneous Catalysis*, 2nd ed.; Ertl, G., Knözinger, H., Schüth, F., Weitkamp, J., Eds.; Wiley: Hoboken, NJ, 2008; Vol. *1*, p 740.
(53) Zhou, K.; Wang, X.; Sun, X.; Peng, Q.; Li, Y. Enhanced Catalytic Activity of Ceria Nanorods from Well-Defined Reactive Crystal Planes. *J. Catal.* **2005**, *229*, 206−212.
(54) Wang, D.; Kang, Y.; Doan-Nguyen, V.; Chen, J.; Küngas, R.; Wieder, N. L.; Bakhmutsky, K.; Gorte, R. J.; Murray, C. B. Synthesis and Oxygen Storage Capacity of Two-Dimensional Ceria Nanocrystals. *Angew. Chem., Int. Ed.* **2011**, *50*, 4378−4381.
(55) Rodriguez, J. A.; Grinter, D. C.; Liu, Z.; Palomino, R. M.; Senanayake, S. D. Ceria-Based Model Catalysts: Fundamental Studies on the Importance of the Metal-Ceria Interface in CO Oxidation, the Water-Gas Shift, CO_2 Hydrogenation, and Methane and Alcohol Reforming. *Chem. Soc. Rev.* **2017**, *46*, 1824−1841.

DOI: 10.1021/acscatal.7b04469
ACS Catal. 2018, 8, 6203−6215

(56) Wu, Z.; Li, M.; Howe, J.; Meyer, H. M., 3rd; Overbury, S. H. Probing Defect Sites on CeO_2 Nanocrystals with Well-Defined Surface Planes by Raman Spectroscopy and O_2 Adsorption. *Langmuir* **2010**, *26*, 16595−16606.
(57) Huang, H.; Dai, Q.; Wang, X. Morphology Effect of Ru/CeO_2 Catalysts for the Catalytic Combustion of Chlorobenzene. *Appl. Catal., B* **2014**, *158*−*159*, 96−105.
(58) Skaf, M.; Hany, S.; Aouad, S.; Gennequin, C.; Labaki, M.; Abi-Aad, E.; Aboukaïs, A. Detection of Adsorbed O_2^- Species on CeO_2 Solid Impregnated with Ag^{2+} Ions during Its Thermal Treatment under A H_2 Atmosphere, An EPR Study. *Phys. Chem. Chem. Phys.* **2016**, *18*, 29381−29386.
(59) Basińska, A.; Jóźwiak, W. K.; Góralski, J.; Domka, F. The Behavior of Ru/Fe_2O_3 Catalysts and Fe_2O_3 Supports in the TPR and TPO Conditions. *Appl. Catal., A* **2000**, *190*, 107−115.
(60) Phanikrishna Sharma, M. V.; Akyurtlu, J. F.; Akyurtlu, A. Autothermal Reforming of Isobutanol over Promoted Nickel Xerogel Catalysts fo Hydrogen Production. *Int. J. Hydrogen Energy* **2015**, *40*, 13368−13378.
(61) Sui, C.; Niu, X.; Wang, Z.; Yuan, F.; Zhu, Y. Activity and Deactivation of Ru Supported on $La_{1.6}Sr_{0.4}NiO_4$ Perovskite-Like Catalysts Prepared by Different Methods for Decomposition of N_2O. *Catal. Sci. Technol.* **2016**, *6*, 8505−8515.
(62) Tang, N.; Cong, Y.; Shang, Q.; Wu, C.; Xu, G.; Wang, X. Coordinatively Unsaturated Al^{3+} Sites Anchored Subnanometric Ruthenium Catalyst for Hydrogenation of Aromatics. *ACS Catal.* **2017**, *7*, 5987−5991.
(63) Ernst, J. B.; Muratsugu, S.; Wang, F.; Tada, M.; Glorius, F. Tunable Heterogeneous Catalysis: N-Heterocyclic Carbenes as Ligands for Supported Heterogeneous Ru/K-Al_2O_3 Catalysts to Tune Reactivity and Selectivity. *J. Am. Chem. Soc.* **2016**, *138*, 10718−10721.
(64) Shang, S.; Zhao, W.; Wang, Y.; Li, X.; Zhang, J.; Han, Y.; Li, W. Highly Efficient Ru@IL/AC to Substitute Mercuric Catalyst for Acetylene Hydrochlorination. *ACS Catal.* **2017**, *7*, 3510−3520.
(65) Liu, X.; Zhang, B.; Xu, L. Nobel Metal Catalyzed Preparation of Ni_2P/α-Al_2O_3. *Phys. Chem. Chem. Phys.* **2013**, *15*, 10510−10514.
(66) Xia, S.; Yuan, Z.; Wang, L.; Chen, P.; Hou, Z. Hydrogenolysis of Glycerol on Bimetallic Pd-Cu/Solid-Base Catalysts Prepared via Layered Double Hydroxides Precursors. *Appl. Catal., A* **2011**, *403*, 173−182.
(67) Binet, C.; Daturi, M.; Lavalley, J.-C. IR Study of Polycrystalline Ceria Properties in Oxidised and Reduced States. *Catal. Today* **1999**, *50*, 207−225.
(68) Laachir, A.; Perrichon, V.; Badri, A.; Lamotte, J.; Catherine, E.; Lavalley, J. C.; El Fallah, J.; Hilaire, L.; Le Normand, F.; Quemere, E.; Sauvion, G. N.; Touret, O. Reduction of CeO_2 by Hydrogen. Magnetic Susceptibility and Fourier-Transform Infrared, Ultraviolet and X-ray Photoelectron Spectroscopy Measurements. *J. Chem. Soc., Faraday Trans.* **1991**, *87*, 1601−1609.
(69) Badri, A.; Binet, C.; Lavalley, J.-C. An FTIR Study of Surface Ceria Hydroxy Groups during a Redox Process with H_2. *J. Chem. Soc., Faraday Trans.* **1996**, *92*, 4669−4673.
(70) Pozdnyakova, O.; Teschner, D.; Wootsch, A.; Krohnert, J.; Steinhauer, B.; Sauer, H.; Toth, L.; Jentoft, F.; Knopgericke, A.; Paal, Z. Preferential CO Oxidation in Hydrogen (PROX) on Ceria-Supported Catalysts, Part I: Oxidation State and Surface Species on Pt/CeO_2 under Reaction Conditions. *J. Catal.* **2006**, *237*, 1−16.
(71) Peden, C. H. F.; Hoffmann, F. M. In-situ FT-IRAS Study of the CO Oxidation Reaction over Ru(001): III. Observation of a 2140 cm^{-1} C-O Stretching Vibration. *Catal. Lett.* **1991**, *10*, 91−101.
(72) Chin, S. Y.; Williams, C. T.; Amiridis, M. D. FTIR Studies of CO Adsorption on Al_2O_3- and SiO_2-Supported Ru Catalysts. *J. Phys. Chem. B* **2006**, *110*, 871−882.
(73) Comas-Vives, A.; Furman, K.; Gajan, D.; Akatay, M. C.; Lesage, A.; Ribeiro, F. H.; Coperet, C. Predictive Morphology, Stoichiometry and Structure of Surface Species in Supported Ru Nanoparticles under H_2 and CO Atmospheres from Combined Experimental and DFT Studies. *Phys. Chem. Chem. Phys.* **2016**, *18*, 1969−1979.
(74) Musolino, M. G.; Caia, C. V.; Busacca, C.; Mauriello, F.; Pietropaolo, R. Selective Conversion of cis-2-butene-1,4-diol to 2-hydroxytetrahydrofuran over K, Ca and Ba Metals-Promoted Ru/SiO_2 Catalysts: Role of the Promoter. *Appl. Catal., A* **2009**, *357*, 106−113.
(75) Li, C.; Sakata, Y.; Arai, T.; Domen, K.; Maruya, K.-i.; Onishi, T. Carbon Monoxide and Carbon Dioxide Adsorption on Cerium Oxide Studies by Fourier-Transform Infrared Spectroscopy. Part 1.-Formation of Carbonate Species on Dehydroxylated CeO_2 at Room Temperature. *J. Chem. Soc., Faraday Trans. 1* **1989**, *85*, 929−943.
(76) Li, C.; Sakata, Y.; Arai, T.; Domen, K.; Maruya, K.-i.; Onishi, T. Adsorption of Carbon Monoxide and Carbon Dioxide on Cerium Oxide Studied by Fourier-Transform Infrared Spectroscopy. Part 2.-Formation of Formate Species on Partially Reduced CeO_2 at Room Temperature. *J. Chem. Soc., Faraday Trans. 1* **1989**, *85*, 1451−1461.
(77) Shido, T.; Iwasawa, Y. Regulation of Reaction Intermediate by Reactant in the Water-Gas Shift Reaction on CeO_2, in Relation to Reactant-Promoted Mechanism. *J. Catal.* **1992**, *136*, 493−503.
(78) Eckle, S.; Anfang, H.-G.; Behm, R. J. Reaction Intermediates and Side Products in the Methanation of CO and CO_2 over Supported Ru Catalysts in H_2-Rich Reformate Gases. *J. Phys. Chem. C* **2011**, *115*, 1361−1367.
(79) Jin, T.; Zhou, Y.; Mains, G. J.; White, J. M. Infrared and X-ray Photoelectron Spectroscopy Study of Carbon Monoxide and Carbon Dioxide on Platinum/Ceria. *J. Phys. Chem.* **1987**, *91*, 5931−5937.
(80) Vayssilov, G. N.; Mihaylov, M.; St. Petkov, P.; Hadjiivanov, K. I.; Neyman, K. M. Reassignment of the Vibrational Spectra of Carbonates, Formates, and Related Surface Species on Ceria: A Combined Density Functional and Infrared Spectroscopy Investigation. *J. Phys. Chem. C* **2011**, *115*, 23435−23454.
(81) Miao, B.; Ma, S. S. K.; Wang, X.; Su, H.; Chan, S. H. Catalysis Mechanisms of CO_2 and CO Methanation. *Catal. Sci. Technol.* **2016**, *6*, 4048−4058.
(82) Wang, F.; He, S.; Chen, H.; Wang, B.; Zheng, L.; Wei, M.; Evans, D. G.; Duan, X. Active Site Dependent Reaction Mechanism over Ru/CeO_2 Catalyst toward CO_2 Methanation. *J. Am. Chem. Soc.* **2016**, *138*, 6298−6305.
(83) Hare, B. J.; Maiti, D.; Daza, Y. A.; Bhethanabotla, V. R.; Kuhn, J. N. Enhanced CO_2 Conversion to CO by Silica-Supported Perovskite Oxides at Low Temperatures. *ACS Catal.* **2018**, *8*, 3021−3029.
(84) Panayotov, D. A.; Yates, J. T. Spectroscopic Detection of Hydrogen Atom Spillover from Au Nanoparticles Supported on TiO_2: Use of Conduction Band Electrons. *J. Phys. Chem. C* **2007**, *111*, 2959−2964.
(85) Lykhach, Y.; Figueroba, A.; Camellone, M. F.; Neitzel, A.; Skála, T.; Negreiros, F. R.; Vorokhta, M.; Tsud, N.; Prince, K. C.; Fabris, S.; Neyman, K. M.; Matolín, V.; Libuda, J. Reactivity of Atomically Dispersed Pt^{2+} Species towards H_2: Model Pt-CeO_2 Fuel Cell Catalyst. *Phys. Chem. Chem. Phys.* **2016**, *18*, 7672−7679.
(86) Chen, H.-Y. T.; Tosoni, S.; Pacchioni, G. Hydrogen Adsorption, Dissociation, and Spillover on Ru_{10} Clusters Supported on Anatase TiO_2 and Tetragonal ZrO_2 (101) Surfaces. *ACS Catal.* **2015**, *5*, 5486−5495.
(87) Boateng, I. W.; Tia, R.; Adei, E.; Dzade, N. Y.; Catlow, C. R. A.; de Leeuw, N. H. A DFT+U Investigation of Hydrogen Adsorption on the $LaFeO_3$(010) Surface. *Phys. Chem. Chem. Phys.* **2017**, *19*, 7399−7409.
(88) Roland, U.; Braunschweig, T.; Roessner, F. On the Nature of Spilt-Over Hydrogen. *J. Mol. Catal. A: Chem.* **1997**, *127*, 61−84.
(89) Castro, G. R.; Drakova, D.; Grillo, M. E.; Doyen, G. A Comparative Theoretical Study of Atomic Hydrogen Adsorption on the (110) Faces of Al, Cu, Ni, and NiAl. *J. Chem. Phys.* **1996**, *105*, 9640−9648.

DOI: 10.1021/acscatal.7b04469
ACS Catal. 2018, 8, 6203−6215